PAN ARCHIVES OF ACOUSTICS
Vol. 39, No. 4, pp. 569–582 (2014)

DOI: 10.2478/aoa-2014-0061

Circular Radon Transform Inversion Technique in Synthetic Aperture Ultrasound Imaging: an Ultrasound Phantom Evaluation

Jurij TASINKEVYCH, Ihor TROTS

Institute of Fundamental Technological Research
Polish Academy of Sciences
Pawińskiego 5B, 02-106 Warszawa, Poland; e-mail: yurijtas@ippt.pan.pl

(*received June 24, 2014; accepted September 30, 2014*)

The paper presents an overview of theoretical aspects of ultrasound image reconstruction techniques based on the circular Radon transform inversion. Their potential application in ultrasonography in a similar way as it was successfully done in the x-ray computer tomography is demonstrated. The methods employing Radon transform were previously extensively explored in the synthetic aperture radars, geophysics, and medical imaging using x-ray computer tomography. In this paper the main attention is paid to the ultrasound imaging employing monostatic transmit-receive configuration. Specifically, a single transmit and receive omnidirectional source placed at the same spatial location is used for generation of a wide-band ultrasound pulse and detection of back-scattered waves. The paper presents derivation of the closed-form solution of the CRT inversion algorithms by two different approaches: the range-migration algorithm (RMA) and the deconvolution algorithm (DA). Experimentally determined data of ultrasound phantom obtained using a 32-element 5 MHz linear transducer array with 0.48 mm element pitch and 0.36 mm element width and 5 mm height, excited by a 2 sine cycles burst pulse are used for comparison of images reconstructed by the RMA, DA, and conventional synthetic aperture focusing technique (SAFT). It is demonstrated that both the RMA and SAFT allow better lateral resolution and visualization depth to be achieved as compared to the DA approach. Comparison of the results obtained by the RMA method and the SAFT indicates slight improvement of the lateral resolution for the SAFT of approximately 1.5 and 1.6% at the depth of 12 and 32 mm, respectively. Concurrently, however, the visualization depth increase for the RMA is shown in comparison with the SAFT. Specifically, the scattered echo amplitude increase by the factor of 1.36 and 1.12 at the depth of 22 and 32 mm is demonstrated. It is also shown that the RMA runs about 30% faster than the SAFT and about 12% faster than the DA method.

Keywords: synthetic aperture focusing method, circular Radon Transform, delay-and-sum beamforming, range migration algorithm.

1. Introduction

In past few decades medical ultrasound imaging has become one of the more prevalent techniques. This is mainly due to its accessibility and lower cost in comparison with computed tomography (CT). For instance, CT scan costs range from 1200 to 3200 $, whereas the ultrasound procedures cost from 100 to 1000 $. Moreover, ultrasound exams do not use ionizing radiation (x-ray) and allow the images to be captured in real-time (rather than after an acquisition or processing delay), showing the structure and movement of the body's internal organs, as well as blood flowing through blood vessels. Ultrasound imaging is usually a painless and portable (it can be brought to a sick person's bedside) medical test that helps physicians diagnose and treat medical conditions. Modern ultrasound scanners employ transducer arrays and advanced beamforming techniques to enhance image quality. Specifically, given the operating frequency, the axial (longitudinal) resolution of the imaging system is defined as half of the spatial pulse length (number of cycles of the emitted pulse times the wavelength). Therefore, the short pulses are usually used (2–3 sine cycles of operating frequency). The axial resolution is depth-independent. On the other hand, the lateral resolution is determined by the width of the emitted wave-beam and directly depends on the transducer aperture size and applied focusing (at specified depth or several depths). The lateral resolution, therefore, is

depth-dependent. Adequate focusing at the whole image space is done at a large cost of slowing the frame rate. Often, this refresh rate is reduced to below 15 fps.

Synthetic aperture (SA) imaging methods offer a solution to this problem. Initially implemented in remote sensing/imaging by radars (Moreira, 1992; Perry, Martinson, 1978) and in sonar imaging (Stergiopoulos, Sullivan, 1989; Yen, Carey, 1989) later they found their application in the ultrasound imaging (Corl *et al.*, 1978; Nagai, 1985; Ozaki *et al.*, 1988), where they are also known as synthetic aperture focusing techniques (SAFT). In SAFT imaging, at each time a single array element acts as a point source emitting a spherical wave to the acoustic medium and as a receiver of the echo signal back-scattered from the inhomogeneities (O'Donnell, Thomas, 1992; Thomson, 1984). To increase emitted energy (which results in signal-to-noise ratio enhancement), a multi-element synthetic aperture focusing (M-SAF), as an alternate to the SAFT method, was proposed (Karaman *et al.*, 1995; Nikolov *et al.*, 1999). A group of elements transmits and receives signals simultaneously. Further improvement of the ultrasound image quality was delivered by the synthetic transmit aperture methods (STA) (Cooley, Robinson, 1994; Lockwood *et al.*, 1998). At each time a single array element (or several elements comprising transmit sub-aperture) transmits an ultrasound pulse and all elements receive the echo signals. The advantage of this approach is that dynamic focusing can be applied in both transmit and receive modes.

The common approach to the synthetic aperture methods is considering the transmit and receive elements (sub-apertures) as point sources. This allows the delay-and-sum (DAS) beamforming technique, based on coherent summing of delayed back-scattered echoes, to be applied. The round-trip echo delays generated by a propagating pulse deliver information about the properties of the media along the path of propagation. Specifically, the received echo signal at each time instant τ (counted from the emission) and receiver spatial position yields an average (integral) of the reflectivity of the media at all spatial points where this wavefront reaches at the specified time instant $\tau/2$ (accounting for the round trip). The time duration and shape of the transmit pulse is usually ignored for simplicity (δ-function approximation). Assuming the spherical wavefront radiating from the transmit element in the case of SAFT imaging (transmit and receive elements coincide) the received signal at each instant is an average of media reflectivity over circular arcs (for STA imaging an elliptical curve path should be considered instead because transmit and receive elements are separated in space). In other words, each pixel of a reconstructed 2D image contains average information about media properties along certain (circular or elliptical) paths. The scattered signals from the reflectors (scatterers) located at these paths are spuriously "transferred" into the focus point, and their influence can not be circumvented. To address this problem, the ultrasound image reconstruction may be formulated in terms of Radon transform inversion. Specifically, the Radon transform can be defined as a set of projections (line integrals) of the function describing certain properties of the object. The problem of determining a function which describes certain properties of the media from knowledge of its line integrals arises in widely diverse fields. These include medical imaging, astronomy, geophysics, optics, electron microscopy, and material science. The general problem of unfolding internal structure of an object by observations of its line integrals is also known as the problem of reconstruction from projections. For example, in x-ray computer tomography (CT) the measured data correspond to projections along straight lines of the x-ray linear attenuation coefficient (under the assumption that x-ray beam consists of mono-energetic photons). In the case of ultrasound imaging what is measured is the back-scattered acoustic wave-field which contains information about the reflectivity coefficient. As it was mentioned above, the SAFT recorded data correspond to the line integrals (projections) along circular arcs and represent the circular Radon transform (CRT) of the reflectivity function.

The aim of this paper is to give an overview of methods related to the Radon transform inversion and their potential application in ultrasonography in a similar way as it was successfully done in the x-ray computer tomography. In particular, the inversion of the circular Radon transform and its application in ultrasound image reconstruction is in the main scope of the present work. In this case the ultrasound image reconstruction can be interpreted as inversion of the CRT represented by recorded back-scattered echo signals. In this paper two imaging algorithms based on the CRT inversion methods are presented. Specifically, the range migration algorithm (RMA) (Cafforio *et al.*, 1991) and deconvolution algorithm (DA) (Norton, 1980) are discussed in detail. The measurement data of tissue phantom and custom design wire phantom obtained using 32-element 5 MHz linear transducer array with 0.48 mm element pitch and 0.36 mm element width and 5 mm height, excited by a 2 sine cycles burst pulse are used for comparison of images reconstructed by the RMA, DA and conventional SAFT methods.

The paper is organized as follows. In the next section a brief review of the SA ultrasound imaging method based on the delay-and-sum approach is given. In Sec. 3 a general discussion regarding the linear Radon transform (LRT) is presented. The CRT inversion algorithms and their relevance to the ultrasound imaging are discussed in Sec. 4. Some examples of ultrasound image reconstruction using measurement

synthetic aperture data are shown in Sec. 5. Finally, in Conclusions a brief summary and possible generalization of the discussed methods of CRT inversion are given.

2. Synthetic Aperture Method

2.1. Synthetic Transmit Aperture algorithm

Regarding the SA methods in ultrasound imaging applications the STA approach is one of the most promising because it enables dynamic focusing both in transmit and receive modes. In the STA method moment of time a single array element acts as a transmitter and all elements receive back-scattered echoes independently, as schematically shown in Fig. 1. For an N-element array, $N \times N$ recordings are required to synthesize a B-mode image. The depth of field is extended without any reduction in frame rate. The focusing is performed by finding the geometric distance from the transmitting element to the imaging point and back to the receiving element, as illustrated in Fig. 2. The data are acquired simultaneously from all directions over a number of emissions, and the full image can be reconstructed from these data. When a short pulse (2–3 sine cycles of operating frequency) is transmitted by

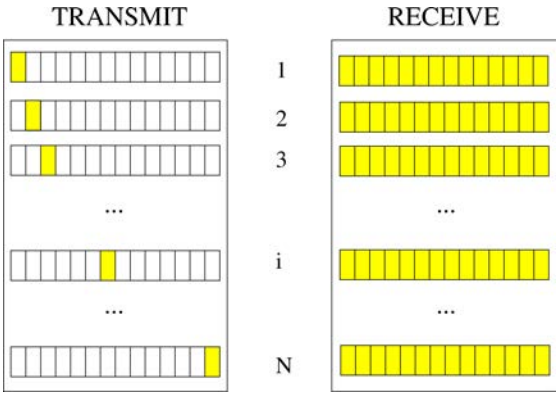

Fig. 1. Transmitting and receiving in the synthetic transmit aperture method.

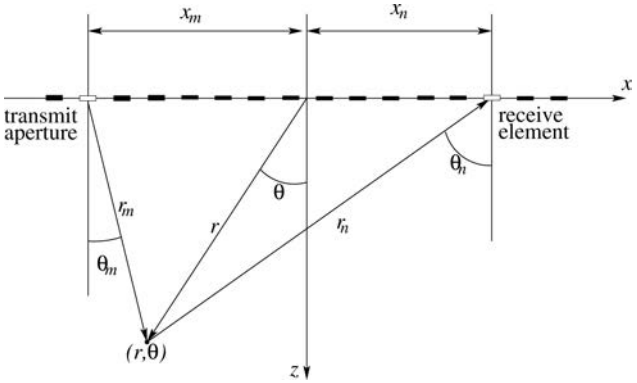

Fig. 2. Transmitting and receiving in the synthetic transmit aperture method.

the element m and the echo signal is received by the element n, as shown in Fig. 2, the round-trip delay is:

$$\tau_{m,n} = \tau_m + \tau_n, \tag{1}$$

where the pair of indexes (m, n) defines the transmit-receive combination, $1 \leq m,\ n \leq N$. Corresponding delays for m-th and n-th elements relative to the imaging point (r, θ) are:

$$\tau_i = \frac{1}{c}\left(r - \sqrt{r^2 + x_i^2 - 2x_i r \sin\theta}\right), \quad i = m, n, \tag{2}$$

where x_m, x_n are the positions of m-th and n-th elements, respectively, and (r, θ) are the polar coordinates of the imaging point with respect to the origin placed in the centre of the transducer's aperture. In the case of an N-element array for each point in the image, the final focused signal can be expressed as follows:

$$A_{\mathrm{STA}}(r,\theta) = \sum_{n=1}^{N}\sum_{m=1}^{N} w_{m,n}(r,\theta) \cdot y_{m,n}(2r/c - \tau_{m,n}(r,\theta)), \tag{3}$$

where $y_{m,n}$ is the received echo signal corresponding to (m, n) transmit-receive pair; $\tau_{m,n}$ is the round-trip delay defined by Eq. (1), evaluated for (m, n) transmit-receive pair at given imaging point (r, θ); $w_{m,n}(r, \theta)$ are the apodization weights (Tasinkevych *et al.*, 2013) accounting for the directivities of the transmit and receive elements. They are evaluated for each transmit-receive combination and each imaging points using the approach for evaluation of the far-field radiation pattern of a periodic array of hard acoustic baffles which model the transducer array (Tasinkevych, 2010; Tasinkevych, Danicki, 2011):

$$w_{m,n}(r,\theta) = f_T(\theta_m) f_R(\theta_n), \quad \theta_i = \theta_i(r,\theta), \qquad i = m, n. \tag{4}$$

In the above equation $\theta_i(r, \theta)$, $i = m, n$ are the observation angles corresponding for the transmit and receive elements, and $f_T(\theta_m)$, $f_R(\theta_n)$ are their directivity functions, respectively. Note, that the angles θ_m and θ_n depend on the spatial position of the focal point (r, θ). In the case of STA algorithm (Tasinkevych *et al.*, 2012) the corresponding directivity function of single-element transmit and receive apertures, which is used for evaluation of weights w_{mn}, can be calculated in the far-field approximation using an analytical expression:

$$f(\theta) = \frac{\sin(\pi d/\lambda \sin\theta)}{\pi d/\lambda \sin\theta}\cos\theta, \tag{5}$$

where d is the element width, and λ is the wavelength. An extra $\cos\theta$ term in the directivity function, Eq. (5), is caused by use of the proper interpretation of the

Rayleigh-Sommerfeld theory (Selfridge *et al.*, 1980). In the case of MSTA method using several elements in transmit mode, however, the analytic formula given by Eq. (5) cannot be used for evaluation of the directivity function. In this case the apodization weights can be successfully evaluated using the approach discussed in detail in (Tasinkevych, Danicki, 2011).

2.2. Synthetic Aperture Focusing Technique

In this Section a special example of the SA method – the SAFT, is briefly discussed. It can be viewed as a particular case of the STA method discussed above. SAFT is a classical synthetic aperture method originating from the early 1960th when it was used for terrain imaging by aircraft-based radars. In this method only a single element acts as both transmitter and receiver on a full array. The active element transmits a short pulse. The back-scattered echo signals are received at the same element and stored in memory for further processing. The same process repeats at all N elements, and an N-element array is synthesized, see Fig. 3. The final synthesized image is obtained by summing of properly delayed and weighted echoes signal. The round trip delays are determined by geometric distance from the active element to imaging point, as illustrated schematically in Fig. 4. Similarly as in the STA, Eqs. (3), the final focused signal can be written as follows:

$$A_{\mathrm{SAFT}}(r,\theta) = \sum_{n=1}^{N} w_n(r,\theta) \cdot y_n(2r/c - 2\tau_n(r,\theta)), \tag{6}$$

where the round trip delay $2\tau_n(r,\theta)$ is given by Eqs. (1) and (2), and the apodization weights $w_n(r,\theta)$ can be determined from Eqs. (4), (5) (see. Fig. 4).

The SAFT algorithm implements the concept of monostatic aperture – the same element in the aperture is used both in transmit and receive modes (in contrast to the STA which is a bistatic one – different elements act as transmitter/receiver pairs). As it will be explained in Sec. 3, the data acquisition scheme realized in the SAFT is directly related to the CRT. Therefore, the image reconstruction may be performed by CRT inversion. In the next section a brief theoretical introduction to the Radon transform is given.

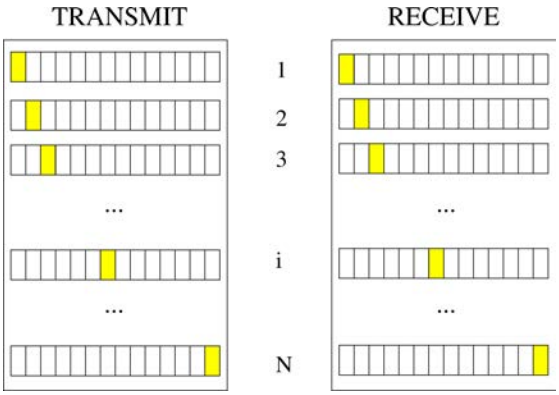

Fig. 3. Transmitting and receiving in synthetic aperture focusing method.

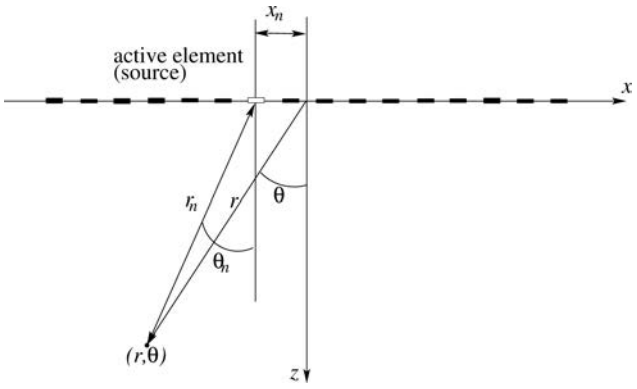

Fig. 4. Transmitting and receiving in synthetic aperture focusing method.

3. Fundamentals of Radon Transform

Before proceeding to the CRT fundamentals it would be helpful to review the basics of the normal Radon transform which represents a set of integrals along straight lines (projections) of certain function describing the object properties. This case will be referred to as the linear Radon transform (LRT) because it is usually written using equation for the line, as explained below. The CRT is a generalization of the LRT and many of the concepts relevant to the CRT may be efficiently explained in the context of the well-established theory of the LRT.

3.1. Linear Radon transform

It was Cormack who in his earlier works (Cormack, 1963; 1964) started a new age in medical diagnostics by applying the inverse of the Radon transform to reconstruct internal images of the body by non-invasive measurements taken from outside the one. He stated that by measuring the intensity of x-ray propagating through the body one obtains the line integrals (projections) of the absorption function. In a simplified form, the measured intensity of the x-ray can be written as follows:

$$I(\theta,\nu) = I_0 \exp\left(-\int_A^B f(x,z)\,\mathrm{d}s\right), \tag{7}$$

and therefore:

$$-\ln\left(\frac{I(\theta,\nu)}{I_0}\right) = \int_A^B f(x,z)\,\mathrm{d}s \equiv p_\theta(\nu) = \mathcal{R}[f](\theta,x'), \tag{8}$$

where $p_\theta(\nu)$ represents a projection of unknown function $f(x,z)$ at the point $x'=\nu$ of the x'-axis rotated by the angle θ; I_0 denotes the emitted x-ray intensity. It should be noted that Eq. (8) holds under assumption of a monoenergetic (in the general case the x-ray linear attenuation coefficient is a function of photon energy) photon beam of an infinitesimal width. The right-hand side of Eq. (8) precisely constitutes a ray (path) integral in that case. The set of projections $p_\theta(\nu)$ is equivalent to the Radon transform of the function $f(x,z)$. Hence, the inverse can be used to reconstruct the original absorption function from the measured data.

Typical definition of the normal Radon transform of the function $f(x,z)$, $x,z\in\mathbb{R}$ is given as its path integral along the straight lines (therefore, it is referred to as linear Radon transform here):

$$g(\theta,x') \equiv \mathcal{R}[f](\theta,x') = \int_{-\infty}^{\infty} f(x'\cos\theta - z'\sin\theta, x'\sin\theta + z'\cos\theta)\,\mathrm{d}z'. \quad (9)$$

Integration in Eq. (9) is performed along the lines parallel to the z'-axis in the Cartesian coordinate system $x'0z'$, rotated by the angle θ with respect to the initial coordinate system $x0z$, see Fig. 5. It is often convenient to rewrite the line integral in Eq. (9) in the form of a double integral as follows:

$$g(\theta,x') \equiv \mathcal{R}[f](\theta,x') = \iint_{-\infty}^{\infty} f(x,z) \cdot \delta(x' - x\cos\theta - z\sin\theta)\,\mathrm{d}x\,\mathrm{d}z, \quad (10)$$

where $\delta(\cdot)$ is the Dirac delta function. Figure 5 illustrates how the set of line integrals of a certain function $f(x,z)$ which represents unknown absorption in the body can be measured by changing the observation angle θ.

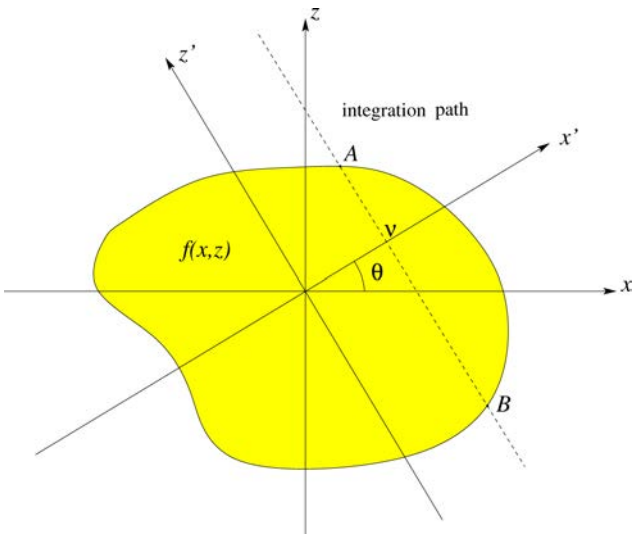

Fig. 5. Radon transform of the function $f(x,z)$ is a set of its path integrals along the straight lines in the rotated Cartesian coordinate system $x'0z'$.

Different approaches of the Radon transform inversion were described in the literature. One of the most elucidated and usually used for image reconstruction in CT is a filtered back-projection approach (Opieliński, Gudra, 2001) which illustrates well the use of the Radon transform and its application. The method employs the projection-slice theorem (Ehrenpreis, 2003), stating that the one-dimensional Fourier transform of any projection $p_\theta(x') \equiv g(\theta,x')$ equals the two-dimensional Fourier transform with respect to the polar coordinates of the unknown function $f(x,z)$:

$$F(\varrho\cos\theta, \varrho\sin\theta) = P_\theta(\varrho), \quad (11)$$

where the two-dimensional Fourier transform is defined as follows:

$$F(k_x,k_z) = \iint_{-\infty}^{\infty} f(x,z) e^{j(k_x x + k_z z)}\,\mathrm{d}x\,\mathrm{d}z \quad (12)$$

and the Fourier transform of the projection $p_\theta(x')$ is:

$$P_\theta(\varrho) = \int_{-\infty}^{\infty} p_\theta(x') e^{j\varrho x'}\,\mathrm{d}x'. \quad (13)$$

To derive the inversion formula one starts from the inverse two-dimensional Fourier transform of the unknown function $f(x,z)$:

$$f(x,z) = \iint_{-\infty}^{\infty} F(k_x,k_z) e^{-j(k_x x + k_z z)}\,\mathrm{d}k_x\,\mathrm{d}k_z \quad (14)$$

which in polar coordinates is:

$$f(x,z) = \int_0^{2\pi}\int_{-\infty}^{\infty} \varrho F(\varrho\cos\theta, \varrho\sin\theta) \cdot e^{-j\varrho(x\cos\theta + z\sin\theta)}\,\mathrm{d}\varrho\,\mathrm{d}\theta. \quad (15)$$

Using Eqs. (11) and (13), the above Eq. (15) can be also written in a slightly different form:

$$f(x,z) = \int_0^{\pi}\int_{-\infty}^{\infty} |\varrho| \left\{ \int_{-\infty}^{\infty} p_\theta(x') e^{j\varrho x'}\,\mathrm{d}x' \right\} \cdot e^{-j\varrho(x\cos\theta + z\sin\theta)}\,\mathrm{d}\varrho\,\mathrm{d}\theta. \quad (16)$$

The above inversion algorithm given by Eq. (16) can be decomposed into two parts. The first step is a high-pass filtering in the spectral domain:

$$\widehat{g}(x',\theta) = \int_{-\infty}^{\infty} |\varrho| \left\{ \int_{-\infty}^{\infty} p_\theta(x') e^{j\varrho x'}\,\mathrm{d}x' \right\} e^{-j\varrho x'}\,\mathrm{d}\varrho, \quad (17)$$

followed by integration of the filtered projections $\widehat{g}(x',\theta)$:

$$f(x,z)=\int_0^{\pi}\widehat{g}(x\cos\theta+z\sin\theta,\theta)\,\mathrm{d}\theta=\int_0^{\pi}\int_{-\infty}^{\infty}\widehat{g}(x',\theta)\cdot\delta(x'-x\cos\theta-z\sin\theta,\theta)\,\mathrm{d}x'\,\mathrm{d}\theta. \tag{18}$$

In the literature Eq. (18) is known as a back-projection and can be regarded as integration along the sinusoidal paths of the filtered projections $\widehat{g}(x',\theta)$.

3.2. Circular Radon Transform

The CRT can be defined in a similar manner as the LRT, Eq. (9) (Agranovsky, Quinto, 1966):

$$g(x_0,r)\equiv\mathcal{R}_c[f](x_0,r)=\int_{L_c}f(x,z)\,\mathrm{d}l, \tag{19}$$

where the path of integration $L_c(x_0,r)$ is a circle of radius r centered at $(x_0,0)$, as illustrated in Fig. 6. The path integral in Eq. (19) can be rewritten in the form of a double integral employing the delta function in a similar manner as in the case of LRT, see Eq. (10):

$$g(x_0,r)\equiv\mathcal{R}_c[f](x_0,r)=\int_{-\infty}^{\infty}\int f(x,z)\cdot\delta(r-\sqrt{z^2+(x-x_0)^2})\,\mathrm{d}x\,\mathrm{d}z. \tag{20}$$

The geometry of CRT shown in Fig. 6 is the most suitable for the SAFT imaging method. Specifically, consider a surface of a two-dimensional reflecting medium $z>0$ and the unidirectional source of ultrasound waves located on the surface at the point $(x_0,0)$ which emits a short pulse wave into the medium and then is switched to the receive mode and acts as a detector of reflected (back-scattered) waves. Assume an infinitesimal time duration of the emitted pulse which means that the source radiates outward expanding circular wavefronts into the media $z>0$. At the time instant r/c, c being the speed of sound in the media, the wavefront reaches the points lying along the circle of radius r and after the further delay of r/c the back-scattered waves arrive back simultaneously at the detector. Therefore, the output signal is proportional to the line integral of the reflectivity function $f(x,z)$ over the semicircular path as shown in Fig. 7a. Moreover, as the radiated circular wavefront continues to propagate into the media, and as the resulting back-scattered echo data are continuously recorded as a function of time, one obtains the family of line integrals of the unknown reflectivity function $f(x,z)$ over an entire family of concentric circles centred at the source location on the surface $(x_0,0)$. Next, the source is translated along the boundary (along the straight line if the linear array transducer is emulated) to the next spatial posi-

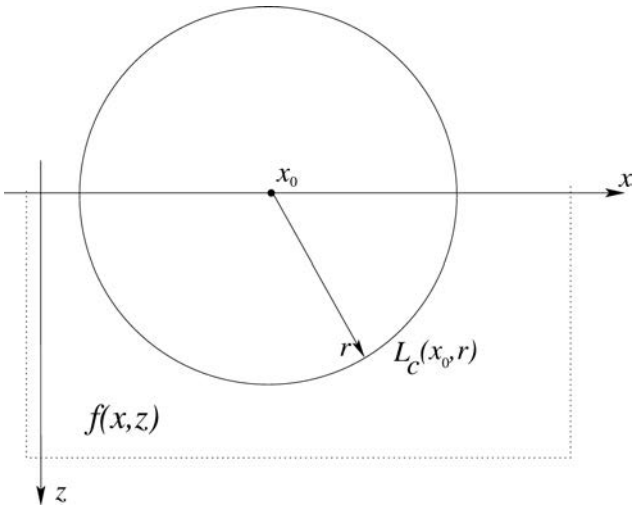

Fig. 6. Circular Radon transform of the function $f(x,z)$ is a set of its path integrals along the circles of radius r centered at $(x_0,0)$.

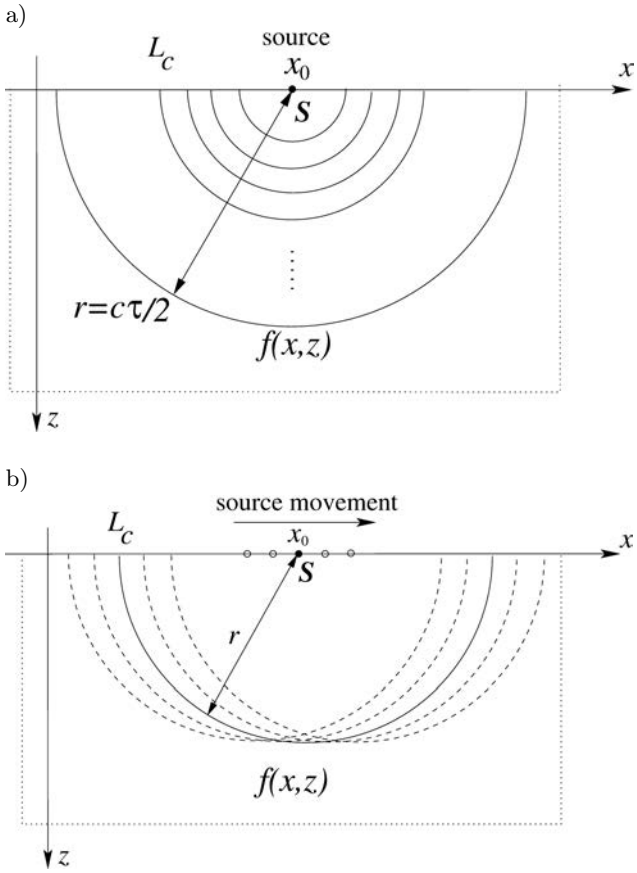

Fig. 7. Geometry of the circular Radon transform relevant to the synthetic aperture focusing imaging method: a) at a given source location on the surface $(x_0,0)$ the received signal at each instant of time is proportional to line integrals of $f(x,z)$ along concentric circles centered at $(x_0,0)$; b) to obtain information about the function $f(x,z)$ over the entire region of interest the source is moved along the boundary and transmit/receive process is repeated.

tion and the transmit-receive process is repeated (see Fig. 7b). Continuing in this way the two-dimensional function $g(x_0, r)$ defined by Eq. (19) is obtained. The transmit-receive process described above corresponds to the SAFT method described in Subsec. 2.2 (see Fig. 3) and the generated set data described by the function $g(x_0, r)$ is the CRT of the unknown reflectivity function $f(x, z)$. Before proceeding to the inversion of the CRT it is worthwhile to remind the main assumptions that were made in the CRT formulation relevant to the SAFT. The speed of sound c and absorption in the medium are assumed constant over the entire region of interest (isotropic and non-dispersive propagating media). Moreover, the generated pulse signal is regarded as a delta function (infinitesimal time duration). This allows a recorded signal at a given time instant τ to be considered as originating from the reflecting objects lying along the semicircular path of the radius $r = c\tau/2$. Finally, the linear dependence between the object function $f(x, z)$, which is related to the characteristics of the reconstructed object, and measured back-scattered field $g(x_0, r)$ is assumed. This approximation, usually applied in the classical image reconstruction problems, means that the multiple-scattering effect in the media is ignored. It always holds in the case of soft biological tissues (and the ultrasound phantom studied in Sec. 5). In the above formulation the image reconstruction problem is obtained by solving the integral equation given by Eq. (19) or its modified version Eq. (20), for unknown reflectivity function $f(x, z)$ in terms of physically recorded data $g(x_0, r)$. This corresponds to the CRT inversion. In the SA ultrasound imaging methods the transducer is usually located on the boundary surface of the acoustic media. Therefore, it is usually reasonable to assume that $f(x, z) = 0$ for $z < 0$ (see Fig. 7).

4. Methods for Inverting the Circular Radon Transform

In this section two examples of CRT inversion algorithms are discussed which are the most relevant to the image reconstruction problem employing the SAFT approach. Both these methods are used in Sec. 5 to obtain the phantom images. Specifically, the range migration algorithm (RMA), considered in Subsec. 4.1, is carried out in the frequency-wavenumber domain thus bringing the benefit of computational efficiency resulting from the use of the fast Fourier transform (FFT) algorithm. It was first introduced as a seismic data processing scheme (Cafforio *et al.*, 1991). Later it was extensively used in the synthetic aperture radars (Milman, 1993), where it is known as the $\omega-k$ migration method. Nowadays it is usually used in geophysics for seismic signal processing, in synthetic aperture radar signal processing, in imaging lidar systems, etc. In Subsec. 4.2 a deconvolution algorithm (DA) of the CRT inversion is discussed (Norton, 1980). The method provides a closed-form analytical solution of the ultrasound image reconstruction problem expressing the reflectivity function in terms of the measured back-scattered field. Specifically, the CRT inversion is reduced to two-dimensional convolution of the measured data with certain kernel function given by an explicit formula. The DA method was chosen because it illustrates well the theoretical foundations of the CRT inverse derivation in the context of the SAFT ultrasound imaging.

4.1. Range Migration Algorithm

The RMA is discussed in this Section following Milman (Milman, 1993). It is convenient to start development of the reconstruction algorithm by rewriting the direct CRT, Eq. (19) as follows:

$$g(x_0, r) = \iint\limits_{(x-x_0)^2+z^2=r^2} f(x, z)\,\mathrm{d}x\,\mathrm{d}z, \tag{21}$$

where the same notation as in Fig. 6 is assumed. To simplify integration in Eq. (21), the following variable transformation can be applied:

$$x = r\tanh\psi + x_0, \qquad z = r\,\mathrm{sech}\,\psi, \tag{22}$$

where the parameter $\psi \in \mathbb{R}$ is defined by the following expression:

$$\sinh\psi = \frac{x - x_0}{z}. \tag{23}$$

Eq. (23) together with Eq. (22) yield the parametric representation $(z\sinh\psi + x, z\cosh\psi)$ of the conjugate hyperbola in the (x_0, r) plane:

$$-\frac{(x - x_0)^2}{z^2} + \frac{r^2}{z^2} = 1, \tag{24}$$

which is the rearranged expression of the circle path integration in Eq. (21). In new variables, defined by Eq. (22), the CRT defined by Eq. (21) can be transformed as follows (note, the Jacobian of the transformation is $-r\,\mathrm{sech}\,\psi$):

$$g(x_0, r) = \int\limits_{-\infty}^{\infty} f(r\tanh\psi + x_0, r\,\mathrm{sech}\,\psi)\, r\,\mathrm{sech}\psi\,\mathrm{d}\psi, \tag{25}$$

Further transformation of Eq. (25) is performed in the spectral domain. To this end the 'range-scaling' of the recorded data is done first:

$$g_0(x_0, r) = \frac{g(x_0, r)}{r}. \tag{26}$$

Then, the two-dimensional Fourier transform of $g_0(x_0, r)$ is evaluated:

$$G_0(k,v) \equiv \mathcal{F}[g_0](k,v) = \iiint_{-\infty}^{\infty} \{f(r\tanh\psi + x_0, r\,\mathrm{sech}\,\psi) r\,\mathrm{sech}\,\psi\,\mathrm{d}\psi\} \cdot e^{j(kx_0+vr)}\,\mathrm{d}x_0\,\mathrm{d}r, \tag{27}$$

where (k, v) is a pair of spectral variables corresponding to the (x_0, r). Noting that (see Eq. (22)):

$$x_0 = x - z\sinh\psi, \qquad r = z\cosh\psi \tag{28}$$

and

$$\mathrm{d}x_0 = \mathrm{d}x, \qquad \mathrm{d}r\,\mathrm{sech}\,\psi = \mathrm{d}z, \tag{29}$$

integration in Eq. (27) can be performed in terms of (x, z) spatial variables, as follows:

$$G_0(k,v) = \iiint_{-\infty}^{\infty} f(x,z) e^{j(vz\cosh\psi - kz\sinh\psi)} \cdot e^{jkx}\,\mathrm{d}\psi\,\mathrm{d}x\,\mathrm{d}z. \tag{30}$$

Applying the Stolt transform (Stolt, 1978) in the Fourier domain: $k_z^2 = v^2 - k^2$ and introducing a new variable φ as follows:

$$\cosh\varphi = \frac{v}{k_z}, \qquad \sinh\varphi = \frac{k}{k_z}, \qquad \varphi \in \mathbb{R}, \tag{31}$$

the two-dimensional Fourier transform, Eq. (30), after a straightforward rearrangement of terms can be rewritten as:

$$G_0(k,k_z) = \iiint_{-\infty}^{\infty} f(x,z) e^{jk_z z\cosh(\psi-\varphi)} \cdot e^{jkx}\,\mathrm{d}\psi\,\mathrm{d}x\,\mathrm{d}z. \tag{32}$$

Using the integral representation of the Hankel functions (Lebedev, 1957a):

$$H_0^{(1)}(z) = \frac{1}{j\pi}\int_{-\infty}^{\infty} e^{jz\cosh\beta}\,\mathrm{d}\beta, \qquad H_0^{(2)}(z) = -\frac{1}{j\pi}\int_{-\infty}^{\infty} e^{-jz\cosh\beta}\,\mathrm{d}\beta, \tag{33}$$

in Eq. (32) one obtains:

$$G_0(k,k_z) = j\pi \iint_{-\infty}^{\infty} H_0^{(1)}(k_z z) f(x,z) e^{jkx}\,\mathrm{d}x\,\mathrm{d}z, \tag{34}$$

where $H_0^{(1)}$ is the Hankel function of the first kind of order 0. Taking into account the definition of integral transform using the Hankel function, Eq. (33), as a kernel (Milman, 1993; Redding, Newsam, 2001):

$$F(s) = \int_{-\infty}^{\infty} H_0^{(1)}(sr) f(r) r\,\mathrm{d}r, \qquad f(r) = \int_{-\infty}^{\infty} H_0^{(2)}(sr) F(s) s\,\mathrm{d}s, \tag{35}$$

it can be shown, that Eq. (34) is equivalent to the Fourier transform with respect to the x_0 spatial variable and the Hankel transform of order zero with respect to z of certain function $f_0(x, z) = f(x, z)/z$. Therefore, the inverse of the above two-dimensional Hankel-Fourier transform yields:

$$f_0(x,z) \equiv \frac{f(x,z)}{z} = \iint_{-\infty}^{\infty} H_0^{(2)}(k_z z) G_0(k,k_z) \cdot e^{-jkx} k_z\,\mathrm{d}k_z\,\mathrm{d}k. \tag{36}$$

Using the first term of asymptotic expansion of the Hankel function $H_0^{(2)}$ (Lebedev, 1957b):

$$H_0^{(2)}(z) \approx \sqrt{\frac{2}{\pi z}} e^{-j(z-\pi/4)}, \tag{37}$$

the stationary phase approximation of Eq. (36) can be obtained:

$$f(x,z) \approx C\sqrt{z} \iint_{-\infty}^{\infty} G_0(k,k_z) e^{-j(kx+k_z z)} \cdot \sqrt{k_z}\,\mathrm{d}k_z\,\mathrm{d}k, \tag{38}$$

where $C = j(1+j)\sqrt{\pi}$. Equation (38) yields the unknown reflectivity function $f(x, z)$ as the inverse two-dimensional Fourier transform of the scaled spectrum $\sqrt{k_z} G_0(k, k_z)$. The RMA can be summarized as follows:

1. Compute the two-dimensional Fourier transform $G_0(k, v)$ of the 'range-scaled' measured data $g_0(x_0, r) = g(x_0, r)/r$.
2. Apply the Stolt transform $k_z^2 = v^2 - k^2$ in the spectral domain by interpolation and resampling the variable v to obtain $G_0(k, k_z)$.
3. Compute the inverse two-dimensional Fourier transform of the scaled spectrum $\sqrt{k_z} G_0(k, k_z)$.
4. Rescale the result of the transformation by factor $\sqrt{z}$ to obtain the unknown reflectivity function $f(x, z)$.

4.2. Deconvolution Algorithm

The DA method is discussed below following Norton (Norton, 1980). By manipulating the Eq. (20)

through a proper change of variables, a closed-form CRT inversion relation in the form of a two-dimensional convolution integral can be derived. A brief development of the inverse CRT is examined below. As shown in (NORTON, 1980) using the following relation:

$$\delta(r-a) = 2r\delta(r^2-a^2). \tag{39}$$

Equation (20) after transformation of the δ-function can be rewritten as:

$$\frac{g(x_0,r)}{r} = 2\iint_{-\infty}^{\infty} f(x,z)\delta(r^2-z^2-(x-x_0)^2)\,\mathrm{d}x\,\mathrm{d}z. \tag{40}$$

Next, introducing new variables:

$$\varrho = r^2, \qquad \xi = z^2$$

the integral in Eq. (40) can be transformed as follows:

$$G(x_0,\varrho) = \iint_{-\infty}^{\infty} F(x,\xi)\delta(\varrho-\xi-(x-x_0)^2)\,\mathrm{d}x\,\mathrm{d}\xi, \tag{41}$$

where the new functions $G(x_0,\varrho)$ and $F(x,\xi)$ were introduced to shorten the notations:

$$G(x_0,\varrho) = \frac{g(x_0,\sqrt{\varrho})}{\sqrt{\varrho}}, \qquad F(x,\xi) = \frac{f(x,\sqrt{\xi})}{\sqrt{\xi}}. \tag{42}$$

Equation (41) is a two-dimensional convolution integral which can be also conveniently written using the symbolic '$**$' notation:

$$G(x_0,\varrho) = F(x_0,\varrho) **\delta(\varrho - x_0^2). \tag{43}$$

Further, the function $F(x_0,\varrho)$ can be expressed as a two-dimensional convolution:

$$F(x_0,\varrho) = G(x_0,\varrho) **R(x_0,\varrho), \tag{44}$$

where the kernel function $R(x_0,\varrho)$ is unknown and has to be determined. Let $G(x_0,\nu)$ and $F(x_0,\nu)$ denote the Fourier transforms of the functions $G(x_0,\varrho)$ and $F(x_0,\varrho)$ with respect to the ϱ. Then, taking into account that the Fourier transform of the δ-function in Eq. (43) is an exponential function in the spectral domain, Eq. (43) can be rewritten as:

$$G(x_0,\nu) = F(x_0,\nu) * e^{j\nu x_0^2}, \tag{45}$$

where the convolution is evaluated with respect to the x_0. To solve Eq. (45) one first evaluates the $G(x_0,\nu) * e^{-j\nu x_0^2}$, which, using the δ-function relation (GEL'FAND, SHILOV, 1964):

$$e^{j\nu x_0^2} * e^{-j\nu x_0^2} = \delta(x_0\nu/\pi) = \frac{\pi\delta(x_0)}{|\nu|} + \frac{\pi\delta(\nu)}{|x_0|}$$

can be rewritten in a symbolic notation as follows:

$$G(x_0,\nu) * e^{-j\nu x_0^2} = \frac{\pi F(x_0,\nu)}{|\nu|} + \pi\delta(\nu)\left(F(x_0,\nu) * \frac{1}{|x_0|}\right). \tag{46}$$

From the above equation, after a rearrangement of the terms, the spectrum $F(x_0,\nu)$ can be determined:

$$F(x_0,\nu) = \frac{1}{\pi}G(x_0,\nu) * \left(|\nu|e^{-j\nu x_0^2}\right) \tag{47}$$

(the second term in Eq. (46) multiplied by $|\nu|$ vanishes). It should be noted that the convolution in Eq. (47) is with respect to the x_0 variable. Comparison of Eq. (47) and Eq. (44) allows the Fourier transform of the function $R(x_0,\varrho)$ with respect to the ϱ variable to be written in the form:

$$R(x_0,\nu) = \pi|\nu|e^{-j\nu x_0^2}. \tag{48}$$

Inverse Fourier transform of Eq. (48) yields the unknown function $R(x_0,\varrho)$ and allows the $F(x_0,\varrho)$ to be determined from Eq. (44), which solves the problem of CRT inversion. Usually, it can be assumed that the physical data are band limited in the sense that $G(x_0,\nu) \approx 0$ for $\nu > \nu_c$, where ν_c is a certain upper limit of the spectrum $G(x_0,\nu)$. In this case, the Fourier transform $G(x_0,\nu)$ can be written as:

$$R(x_0,\nu) = \pi|\nu|\mathrm{rect}(\nu/2\nu_c)e^{-j\nu x_0^2}, \tag{49}$$

where the $\mathrm{rect}(s) = 1$ for $|s| < 1/2$ and 0 otherwise. It can be shown that the closed-form analytical expression can be obtained for the inverse Fourier transform of Eq. (49) as follows (NORTON, 1980):

$$R(x_0,\varrho) = \pi\nu_c\left\{2\mathrm{sinc}\big(2\nu_c(\varrho+x_0^2)\big) - \mathrm{sinc}^2\big(\nu_c(\varrho+x_0^2)\big)\right\}, \tag{50}$$

where $\mathrm{sinc}u = \sin(\pi u)/(\pi u)$ is the normalized sinc function. On substitution of Eq. (50) into Eq. (42) and recalling that $\varrho = r^2$ and $\xi = z^2$, the expression for the reflectivity function $f(x,z)$ can be written as the two-dimensional convolution:

$$f(x,z) = \pi z\nu_c^2 \iint_{-\infty}^{\infty} g(x_0,r) \cdot \left\{2\mathrm{sinc}\left(2\nu_c(z^2-r^2+(x-x_0)^2)\right) - \mathrm{sinc}^2\left(\nu_c(z^2-r^2+(x-x_0)^2)\right)\right\}\mathrm{d}r\,\mathrm{d}x_0. \tag{51}$$

Therefore, the DA method discussed above can be summarized as follows:

1. Apply the change of variable $\varrho = r^2$ and range scale the measured data:

$$G(x_0,\varrho) = g_0(x_0,\sqrt{\varrho})/\sqrt{\varrho}.$$

2. Compute the 'kernel' $R_0(x_0, \varrho)$ using Eq. (50).
3. Compute the two-dimensional convolution:

$$F(x,\xi) = \int\int_{-\infty}^{\infty} G(x_0,\varrho) R_0(x - x_0, \xi - \varrho)\,\mathrm{d}x_0\,\mathrm{d}\varrho.$$

4. Perform the change of variable and rescale the result by factor z to obtain the unknown reflectivity function $f(x,z) = zF(x,z^2)$.

Usually, the two-dimensional convolution in step 3 is computed using the convolution theorem applied to the two-dimensional Fourier transforms of $G(x_0, \varrho)$ and $R_0(x_0, \varrho)$.

5. Numerical Results and Discussion

In this Section the CRT inversion algorithms, discussed in the previous Section (the RMA and DA methods), are implemented and tested. Specifically, the numerical examples of image reconstruction of experimentally determined ultrasound phantom data (Dansk Fantom Service, model 525 (Phantom, 525)) are illustrated in Figs. 8 and 9. All images are displayed in logarithmic scale over 30 dB dynamic range which approximately corresponds to the level of the noise-like spatial fluctuations of the recorded back-scattered echoes (as illustrated in Fig. 11 for the depths exceeding 40 mm). A 32-element 5 MHz linear transducer array with 0.48 mm element pitch and 0.36 mm element width and 5 mm height, excited by 2 sine cycles burst pulse, was used in the measurements. The RF data collected on each of 32 receive channels were digitized at a 12-bit resolution and 50 MHz temporal sampling

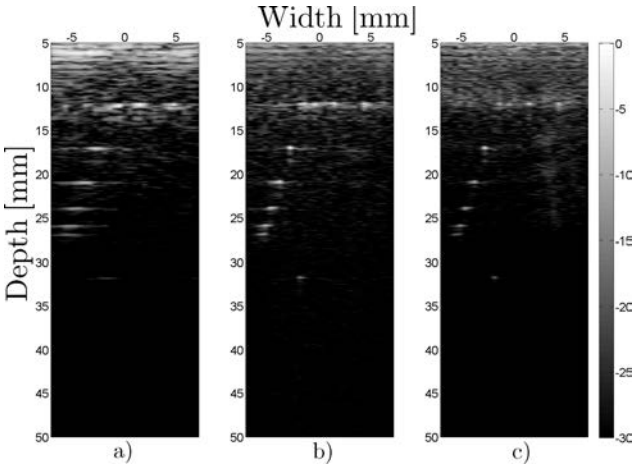

Fig. 8. Image reconstruction of the measurement synthetic aperture data for the ultrasound phantom (Dansk Fantom Service, model 525) and 5 MHz 32-element transducer array with 0.48 mm pitch: a) deconvolution method, b) range migration method, c) conventional synthetic aperture focusing method. All images are displayed over 30 dB dynamic range.

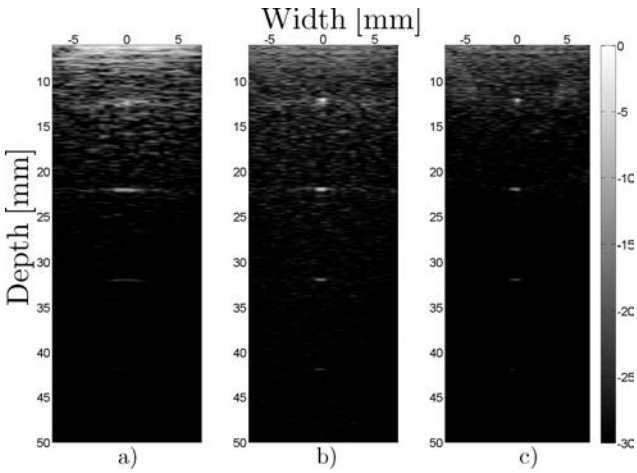

Fig. 9. Image reconstruction of the measurement synthetic aperture data for the ultrasound phantom (Dansk Fantom Service, model 525) and 5 MHz 32-element transducer array with 0.48 mm pitch: a) deconvolution method, b) range migration method, c) conventional synthetic aperture focusing method. All images are displayed over 30 dB dynamic range.

rate and transferred to a PC for further off-line processing in Matlab® in order to test the image reconstruction algorithms. The processing time in Matlab® 7.11 on a PC running Windows 7 x64 with Athlon 64 X2 Dual Core 5600+, core speed 2.8 MHz, was about 0.88 s for the SAFT, 0.69 s for DA, and 0.61 s for the RMA method.

The two-dimensional direct and inverse Fourier transforms in Eq. (27) and Eq. (38) in the RMA approach, as well as the two-dimensional convolution (using convolution theorem for Fourier transform) in the DA method, Eq. (44), were evaluated by means of the FFT algorithm. In the numerical examples shown below the FFT2 Matlab® routine was used to this end. The variable transforms were required in both the RMA (range-scaling, Eq. (26), and Stolt transform, Eq. (31)) and DA methods (geometrical distortion of measured data and rescaling of a reconstructed function, Eq. (41)). This usually means that some interpolation scheme has to be implemented to evaluate the corresponding functions on a uniformly sampled rectangular grids, as required by the FFT2 routine. In the numerical examples shown in this Section the linear interpolation was employed using the Matlab® INTERP2 routine.

By visual assessment of the image reconstruction results illustrated in Fig. 8 and Fig. 9 one can conclude that DA approach yields much worse lateral resolution in comparison with the RMA and SAFT methods. This is further illustrated in Fig. 10 where the resolution capabilities of different approaches are indicated.

Specifically, in Fig. 10a and 10b the lateral cross-sections of the images shown in Fig. 9 at the depths of 12 and 32 mm obtained using the range migration (the

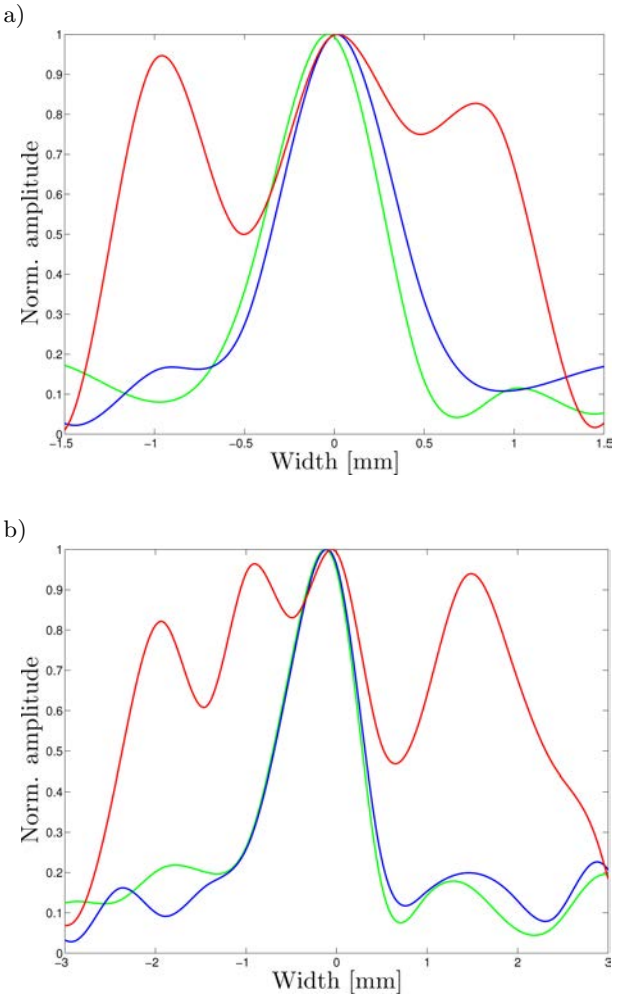

Fig. 10. Normalized lateral cross-sections of the image shown in Fig. 9 for reflectors at different depths: a) 12 mm, b) 32 mm; the green line – demonstrates shows corresponds to the range migration method, the blue line – demonstrates shows corresponds to the synthetic aperture focusing method, the red line – demonstrates shows corresponds to the deconvolution method.

green line), the synthetic aperture (the blue line) and the deconvolution (the red line) methods can be found. As illustrated in Fig. 10, for the RMA approach the lateral resolution is slightly decreased in comparison with the one obtained by using the SAFT. It is quantified here by the full width at half maximum (FWHM). Accordingly, at the axial distance of 12 and 32 mm for the RMA, the lateral resolution is 0.6943 and 0.9153 mm, respectively. The corresponding data for the SAFT are 0.6833 and 0.9014 mm, which represent 1.5 and 1.6% increase in the lateral resolution at the above identified depths. In the case of the DA method the lateral resolution at the depth of 12 and 32 mm is equal to 2.33 and 2.26 mm, respectively. These represent the decrease by the factor of 3.4 and 2.5 in comparison with the SAFT and by the factor of 3.36 and 2.47 in comparison with the RMA approach at the above depths.

In Fig. 11 the normalized axial cross-sections of the central column of reflectors shown in Fig. 9 in a logarithmic scale are illustrated. The scattered echo amplitudes at the depth of 22 and 32 mm obtained using the SAFT method (the blue line) are decreased by −8.76 and −15.3 dB in comparison with the reference depth 12 mm. The corresponding data for the RMA (the green line) are −6.17 and −14.27 dB, which reveals a slight improvement of visualization depth for the RMA as compared to the SAFT. For the DA approach (the red line) the scattered echo amplitudes at the specified depths are −5.17 and −17.7 dB, which indicates the fastest decrease of the scattered amplitude with depth. The already mentioned increase in the visualization depth for the RMA method is further illustrated in Fig. 12 where a detailed view of the axial cross-sections (central column) showing the maxima of the scattered echo signals as a function of depth are presented.

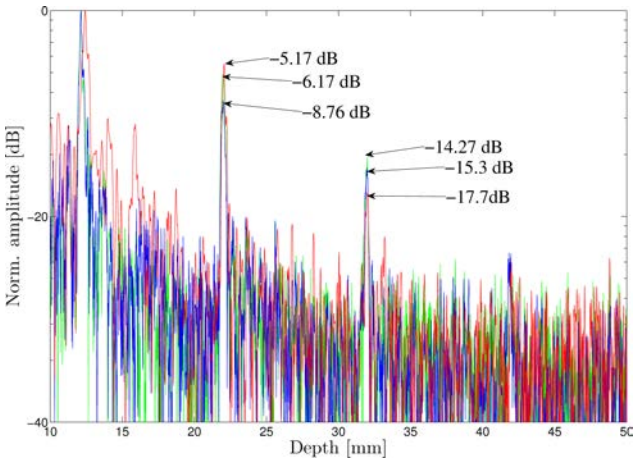

Fig. 11. Normalized axial cross-section (in logarithmic scale) of the central column of reflectors shown in Fig. 9; the green line – demonstrates shows corresponds to the range migration method, the blue line – demonstrates shows corresponds to the synthetic aperture focusing method, the red line – demonstrates shows corresponds to the deconvolution method.

As shown in Figs. 12a and 12b in comparison with the SAFT, the scattered echo amplitudes at the depth of 22 and 32 mm obtained using the RMA algorithm are 1.36 and 1.12 times larger, respectively. On the other hand, at the depth of 22 mm the DA method yields increase of the scattered amplitude by the factor of 1.52 as compared to the SAFT and by the factor of 1.12 as compared to the RMA. But at the depth of 32 mm the corresponding amplitude is 1.3 and 1.46 times smaller in comparison with the SAFT and RMA approaches, respectively. This indicates the fastest scattered amplitude decrease and the lowest visualization depth achievable by the DA method.

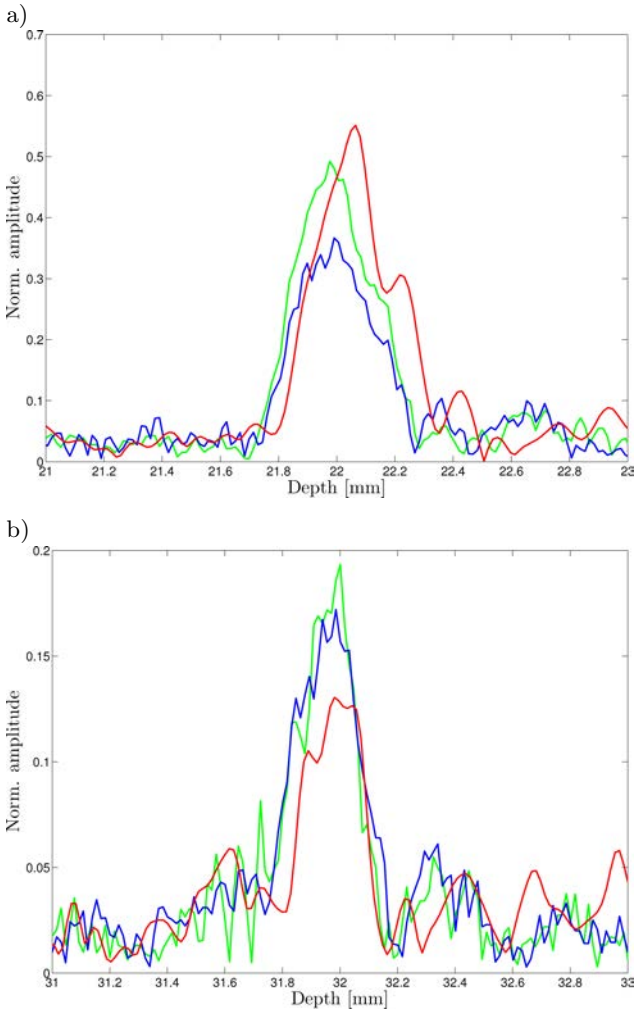

Fig. 12. Normalized axial cross-sections of the image line coinciding with the central column of point reflectors (see Fig. 9) at different depths: a) 22 mm, b) 32 mm; the green line – demonstrates shows corresponds to the range migration method, the blue line – demonstrates shows corresponds to the synthetic aperture focusing method, the red line – demonstrates shows corresponds to the deconvolution method.

6. Conclusions

In this paper the ultrasound imaging techniques based on the CRT inversion were presented. The image reconstruction problem discussed here is based on the assumption that a short ultrasound pulse is transmitted into the acoustic media and back-scattered echoes are received by omnidirectional element. Moreover, the spatial locations of the source and detector coincide. In this case the measured data yield the line integrals along circular arcs of an acoustic reflectivity function. The reconstruction problem was formulated as a linear integral relation between the measured data $g(x_0, r)$ and unknown reflectivity $f(x, z)$. Two different methods of the CRT inversion were considered: the range-migration algorithm by Milman (1993) and deconvolution algorithm by Norton (1980) and compared to the standard monostatic SA method – the SAFT.

In the RMA method the recorded back-scattered echo signals $g(x_0, r)$ were first range-scaled using Eq. (26) yielding $g_0(x_0, \varrho)$. Then the two-dimensional Fourier transform $G_0(k, v)$ was evaluated using the FFT algorithm. The change of variable $k_z^2 = v^2 - k^2$ in the Fourier domain allowed the unknown reflectivity function $f(x, z)$ to be obtained from the relation Eq. (38) which was then rescaled by a $\sqrt{z}$ two-dimensional inverse Fourier transform of the function $\sqrt{k_z} G_0(k, k_z)$. In the DA approach the measurement data $g(x_0, r)$ were first geometrically distorted using Eq. (41) yielding $G(x_0, \varrho)$. Then the function $F(x, \xi)$ was obtained from the two-dimensional convolution relation Eq. (44), which was evaluated using the convolution theorem for the Fourier transform in the numerical examples presented in Sec. 5. Finally, the reconstruction of the reflectivity function $f(x, z)$ was obtained from $F(x_0, \xi)$ through Eq. (41).

In the considered algorithms the main difficulties were introduced by the variable transformation in the spatial and spectral domains. The range-scaling of the measured data $g(x_0, r)$ (normally sampled in uniform increments in the radial direction) was done using INTERP2 routine in Matlab® to evaluate $g_0(x_0, \varrho)$ in the RMA using Eq. (26) and $G(x_0, \varrho)$ in the case of DA from Eq. (41) on a uniform grid. Moreover, in the case of the RMA approach the same routine was called for interpolation of the uniformly sampled spectrum function $G_0(k, v)$ in the Fourier domain to obtain the values of the function $G_0(k, k_z)$ at the nodes of the rectangular grid, so that the inverse FFT algorithm could be applied in Eq. (38).

It was demonstrated, that the images of ultrasound phantom (Phantom, 525) obtained using the RMA as well as the SAFT methods provided a considerable improvement of the lateral resolution and a slight improvement of the visualization depth in comparison with the DA method. Specifically, at the depth of 12 and 32 mm the increase of the lateral resolution by the factor of 3.4 and 2.5 was demonstrated for the conventional SAFT and by the factor of 3.36 and 2.47 for the RMA. Also, the visualization depth was lower for the DA method in comparison with the RMA and the SAFT. Specifically, the fastest decrease of the scattered echo amplitude as a function of depth was demonstrated. More specifically, at the depth of 32 mm the scattered amplitude was 1.3 times larger for the SAFT and 1.46 times larger for the RMA methods in comparison with the DA.

It was also shown that using the RMA algorithm a slight increase of the visualization depth can be achieved, as compared to the SAFT method. Specifically, the scattered echo amplitude at the depth of 22 and 32 mm was 1.36 and 1.12 times larger for the images obtained using the RMA method in comparison

with the SAFT. Moreover, the RMA ran about 30% faster than the SAFT and about 12% faster than the DA method. Concurrently, however, a slight degradation of the lateral resolution was observed; namely, at the depth of 12 and 32 mm the SAFT method provided the lateral resolutions, which was 1.5 and 1.6% better, respectively, than the one achieved with the RMA method.

The image reconstruction algorithms based on the CRT inversion considered in this paper correspond to the monostatic SA imaging method – the SAFT. To enable them to be applied in clinical applications for real-time ultrasound imaging their further development is required to obtain algorithms of reconstructing the unknown reflectivity function given by its line integrals over elliptical paths. This corresponds to the case of bistatic transmit-receive scheme appropriate to the STA and MSTA ultrasound imaging methods (Tasinkevych *et al.*, 2012; 2013), which seems to be promising to be employed in clinical examinations. In this case the ultrasound image reconstruction problem can be formulated in terms of the elliptic Radon transform inversion (ERT) (Moon, 2014). The discussed in this paper RMA method, which involves the Hankel transform seems to be the most suitable to be generalized for development of the ERT inversion algorithm. This is a subject for further research.

Finally, it should be outlined that the derivation of the two-dimensional solution can be straightforwardly generalized to three dimensions. In this case, the line integrals over circles become surface integrals over spheres, the double convolutions become triple convolutions, and the data recording aperture becomes a two-dimensional matrix transducer (Danicki, Tasinkevych, 2012) instead of a linear array transducer.

Acknowledgment

This work was supported by the Polish Ministry of Science and Higher Education (Grant NO. N515 500540).

References

1. Agranovsky M.L., Quinto E.T. (1996), *Injectivity sets for the Radon transform over circles and complete systems of radial functions*, J. Funct. Anal., **139**, 383–413.

2. Cafforio C., Prati C., Rocca F. (1991), *SAR data focusing using seismic migration techniques*, IEEE Trans. Aerosp. Electron. Syst., **27**, 194—207.

3. Cooley C., Robinson B. (1994), *Synthetic focus imaging using partial datasets*, Proc. 1994 IEEE Ultrason. Symp., **3**, 1539–1542.

4. Corl P.D., Grant P.M., Kino G. (1978), *A Digital Synthetic Focus Acoustic Imaging System for NDE*, Proc. 1978 IEEE Ultrason. Symp., 263–268.

5. Cormack A.M. (1963), *Representation of a function by its line integrals, with some radiological applications*, J. Appl. Phys., **34**, 9, 2722–2727.

6. Cormack A.M. (1964), *Representation of a function by its line integrals, with some radiological applications. II*, J. Appl. Phys., **35**, 10, 2908–2913.

7. Danicki E., Tasinkevych Y. (2012), *Acoustical Imaging*, vol. 31, Chap. Beam-forming electrostrictive matrix, Springer, 363–369.

8. Ehrenpreis L. (2003), *The Universality of the Radon Transform*, Chap. 1.7, Clarendon Press Oxford, 87.

9. Gel'fand I.M., Shilov G.E. (1964), *Generalized Functions*, Chap. III, New York: Academic Press, 329.

10. Karaman M., Li P.C., O'Donnell M. (1995), *Synthetic aperture imaging for small scale systems*, IEEE Trans. Ultrason., Ferroelectr. Freq. Contr., **42**, 3, 429–442.

11. Lebedev N.N. (1957a), *Special Functions and Their application (in Polish)*, Chap. V, PWN Warsaw, 126.

12. Lebedev N.N. (1957b), *Special Functions and Their application (in Polish)*, Chap. V, PWN Warsaw, 130.

13. Lockwood G.R., Talman J.R., Brunke S.S. (1998), *Real-time 3-D ultrasound imaging using sparse synthetic aperture beamforming*, IEEE Trans. Ultrason., Ferroelectr. Freq. Contr., **45**, 4, 980–988.

14. Milman A.S. (1993), *SAR imaging by $\omega-k$ migration*, Int. J. Remote Sens., **14**, 10, 1965–1979.

15. Moon S. (2014), *On the determination of a function from an elliptical Radon transform*, Journal of Mathematical Analysis and Applications, **416**, 2, 724–734.

16. Moreira A. (1992), *Real-time synthetic aperture radar (SAR) processing with a new subaperture approach*, IEEE Trans. Geosci. Remote Sens., **30**, 4, 714–722.

17. Nagai K. (1985), *A New Synthetic-Aperture Focusing Method for Ultrasonic B-Scan Imaging by the Fourier Transform*, IEEE Trans. Sonics Ultrason., **32**, 4, 531–536.

18. Nikolov S., Gammelmark K., Jensen J. (1999), *Recursive ultrasound imaging*, Proc. 1999 IEEE Ultrason. Symp., vol. 2, 1621–1625.

19. Norton S.J. (1980), *Reconstruction of a reflectivity field from line integrals over circular paths*, J. Acoust. Soc. Am., **67**, 3, 853–863.

20. O'Donnell M., Thomas L.J. (1992), *Efficient synthetic aperture imaging from a circular aperture with possible application to catheter-based imaging*, IEEE Trans. Ultrason., Ferroelectr. Freq. Contr., **36**, 3, 366–380.

21. Opieliński K.J., Gudra T. (2001), *Industrial and Biological Tomography – Theoretical Basis and Applications*, Chap. Ultrasonic transmission tomography, Electrotechnical Institute, Warsaw, 275–276.

22. Ozaki Y., Sumitani H., Tomoda T., Tanaka M. (1988), *A new system for real-time synthetic aperture ultrasonic imaging*, IEEE Trans. Ultrason., Ferroelectr. Freq. Contr., **35**, 6, 828–838.

23. Perry R.M., Martinson L.W. (1978), *Radar Technology*, Chap. Radar matched filtering, Artech House, Boston, 163–169.

24. Phantom (525), http://www.fantom.dk/525.htm.

25. Redding N.J., Newsam G.N. (2001), *Inverting the Circular Radon Transform*, DTSO Research Raport DTSO-RR-0211.

26. Selfridge A.R., Kino G.S., Khuriyakub B.T. (1980), *A theory for the radiation pattern of a narrow-strip acoustic transducer*, Appl. Phys. Lett., **37**, 1, 35–36.

27. Stergiopoulos S., Sullivan E.J. (1989), *Extended towed array processing by an overlap correlator*, J. Acoust. Soc. Am., **86**, 1, 158–171.

28. Stolt R.H. (1978), *Migration by Fourier transform*, Geophysics, **43**, 23–48.

29. Tasinkevych Y. (2010), *Wave generation by a finite baffle array in applications to beam-forming analysis*, Archives of Acoustics, **35**, 4, 677–686.

30. Tasinkevych Y., Danicki E.J. (2011), *Wave generation and scattering by periodic baffle system in application to beam-forming analysis*, Wave Motion, **48**, 2, 130–145.

31. Tasinkevych Y., Klimonda Z., Lewandowski M., Nowicki A., Lewin P.A. (2013), *Modified multi-element synthetic transmit aperture method for ultrasound imaging: A tissue phantom study*, Ultrasonics, **53**, 570–579.

32. Tasinkevych Y., Trots I., Nowicki A., Lewin P.A. (2012), *Modified synthetic transmit aperture algorithm for ultrasound imaging*, Ultrasonics, **52**, 2, 333–342.

33. Thomson R.N. (1984), *Transverse and longitudinal resolution of the synthetic aperture focusing technique*, Ultrasonics, **22**, 1, 9–15.

34. Yen N.C., Carey W. (1989), *Application of synthetic aperture processing to towed-array data*, J. Acoust. Soc. Am., **86**, 2, 754–765.